Twenty-Four-Hour Raman Lidar Water Vapor Measurements during the Atmospheric Radiation Measurement Program's 1996 and 1997 Water Vapor Intensive Observation Periods

D. D. TURNER

Pacific Northwest National Laboratory, Richland, Washington

J. E. M. GOLDSMITH

Sandia National Laboratories, Livermore, California

(Manuscript received 13 May 1998, in final form 8 September 1998)

ABSTRACT

Prior to the Atmospheric Radiation Measurement program's first water vapor intensive observation period (WVIOP) at the Cloud and Radiation Testbed site near Lamont, Oklahoma, an automated 24-h Raman lidar was delivered to the site. This instrument, which makes high-resolution measurements of water vapor both spatially and temporally, is capable of making these measurements with no operator interaction (other than initial start-up) for days at a time. Water vapor measurements collected during the 1996 and 1997 WVIOPs are discussed here, illustrating both the nighttime and daytime capabilities of this system. System characteristics, calibration issues, and techniques are presented. Finally, detailed intercomparisons of the lidar's data with those from a microwave radiometer, radiosondes, an instrumented tower, a chilled mirror flown on both a tethersonde and kite, and measurements from aircraft are shown and discussed, highlighting the accuracy and stability of this system for both nighttime and daytime measurements.

1. Introduction

Water vapor is the most important greenhouse gas in the atmosphere, as it is the most active infrared absorber and emitter of radiation. It also plays a very important role in energy transport and cloud formation. Atmospheric processes involving water vapor are among the most difficult to model, yet any global warming scenario must take into account both the spatial and temporal variation of this gas in order to properly account for it. Therefore, accurate high-resolution measurements of this variable are critical to improve our understanding of these processes and thus our ability to model them.

Several experiments have shown that Raman lidars can provide these high-resolution measurements. Raman lidar measurements of water vapor were first made by Melfi et al. (1969) and Cooney (1970), and methods and instrumentation have improved greatly since these initial measurements. Now, the evolution of water vapor fields and synoptic events such as cold fronts can be measured in detail by Raman lidars (Melfi and Whiteman 1985; Melfi et al. 1989). Initially, Raman lidars were operated only at night, since the large solar background during the day hampers the detection of the relatively weak Raman backscattered signal. A Raman lidar, specifically built for the Department of Energy's Atmospheric Radiation Measurement (ARM) program by Sandia National Laboratories (Goldsmith et al. 1998) to address the water vapor measurement requirements of the ARM program (Stokes and Schwartz 1994), was designed to profile continuously *throughout* the diurnal cycle in an *autonomous* manner using dual fields of view and narrowband interference filters. The ability to make automated 24-h water vapor measurements for days at a time makes this lidar system unique.

This Raman lidar completed the complement of water vapor instruments at the ARM Southern Great Plains (SGP) Cloud and Radiation Testbed (CART) site near Lamont, Oklahoma. Other water vapor instruments at the site include a two-channel microwave radiometer (Radiometrics WVR-1100), high-quality in situ point sensors (Vaisala HMP35D) on an instrumented tower, and a radiosonde launch site from which up to eight radiosondes (Vaisala RS80-15LH) are launched daily. Further information about these instruments can be found on the ARM instrument Web site (http://www.arm.gov/docs/instruments.html).

The ARM program, recognizing the need both within

Corresponding author address: D. D. Turner, Pacific Northwest National Laboratory, P.O. Box 999, MS K7-28, Richland, WA 99352. E-mail: dave.turner@pnl.gov

and outside the ARM community to improve and validate state-of-the-art measurements in water vapor, initiated a series of three water vapor intensive observation periods (WVIOPs) at its SGP CART site. The first WVIOP was held during September 1996, with the second intensive observation period (IOP) occurring in September–October 1997. Additional instrumentation was brought to the CART site to provide measurements of water vapor during these three-week IOPs and to help characterize the CART instrumentation. In particular, the National Aeronautics and Space Administration (NASA)/Goddard Space Flight Center's scanning Raman lidar (Whiteman et al. 1992; Ferrare et al. 1992) was present, providing high-resolution water vapor and aerosol profiles primarily during the night. A tethersonde system from Los Alamos National Laboratory was flown with a chilled mirror hygrometer from the surface up to a maximum altitude of 1 km (depending on wind speed), and a kite from the University of Colorado was used to carry the chilled mirror hygrometer if winds were too high to fly the tethersonde. During the second WVIOP, in situ humidity measurements were made by the University of North Dakota Citation and Pacific Northwest National Laboratory Gulfstream aircraft. These and other instruments complemented the standard CART measurements and provided an excellent opportunity to calibrate and characterize the CART Raman lidar.

In this paper, we discuss how we calibrated the water vapor mixing ratio profiles derived from the CART Raman lidar, as well as discuss some issues involved in this. We then present some data collected during both IOPs and discuss the comparison of the lidar's data with the other water vapor measurements. In particular, emphasis is placed on the lowest kilometer and upper troposphere, the focus of the first and second WVIOPs, respectively. Focus is also placed on the daytime measurements. Comparisons with the NASA/Goddard Space Flight Center's Raman lidar, which requires detailed information about both lidar systems in order to understand the results, will be the subject of another paper and are not discussed here. Finally, the lessons learned from this study and plans for future research will be presented.

2. Raman lidar operation

a. Theory

Most lidar systems operate by transmitting a laser pulse into the atmosphere and recording the backscattered light as a function of time. Since normal Raman scattering is nonresonant, the wavelength of the outgoing laser beam is arbitrary, and the choice of the wavelength transmitted can be made to optimize the system in other ways (Goldsmith et al. 1998). Using the Stokes component of Raman scattering, the energy shifts—which are unique for different molecular species—associated with water vapor and nitrogen are 2329 and 3654 cm^{-1}, respectively. These relatively large energy shifts allow the use of dichroic mirrors to separate the wavelengths into separate channels for detection. Narrowband interference filters are used to select only the wavelengths of choice, and photomultiplier tubes are used to measure the backscattered intensity in photon counting mode.

The signal for each of these channels is described by the lidar equation (Measures 1984) given in Eq. (1):

$$S_j(r) = k_j r^{-2} O_j(r) \sigma_j n_j(r) q(\lambda_0, r) q(\lambda_j, r), \qquad (1)$$

where S_j is the received signal in channel j as a function of range r, O_j is the optical overlap function describing the detector's field of view, σ_j is the Raman cross section for the species detected in channel j, n_j is the number density of that species, $q(\lambda_0, r)$ describes the transmission of the outgoing laser beam, and $q(\lambda_j, r)$ describes the transmission of the backscattered signal. The Raman cross section σ_j does have a temperature dependence and thus, there is some dependence on altitude, although at atmospheric temperatures these cross sections are relatively constant (Whiteman et al. 1993). The constant k_j includes the laser pulse energy, the receiver's area, and the overall sensitivity of the channel.

The water vapor mixing ratio is defined to be the ratio of the mass of water vapor to the mass of dry air in a given volume, which is proportional to the number density of water molecules to the number density of nitrogen molecules. By taking the ratio of the water vapor and nitrogen channel signals, as illustrated in Eq. (2),

$$\frac{S_{\mathrm{wv}}(r)}{S_{\mathrm{nit}}(r)} = kO(r) \frac{n_{\mathrm{wv}}(r) q(\lambda_{\mathrm{wv}}, r)}{n_{\mathrm{nit}}(r) q(\lambda_{\mathrm{nit}}, r)}, \qquad (2)$$

many of the terms in the equation are eliminated (such as the range-squared dependence, the area of the receiver, the energy of the laser, and the transmission at the laser's wavelength), with the various constants gathered into k and the ratio of the optical overlap functions for each channel represented by $O(r)$. Therefore, by specifying $O(r)$ and $q(\lambda_{\mathrm{wv}}, r)/q(\lambda_{\mathrm{nit}}, r)$, the ratio of the signals from the two channels is proportional to the water vapor mixing ratio. These corrections, which are part of the calibration sequence, are discussed in more detail in section 3.

b. System details

The CART Raman lidar uses a frequency tripled Nd:YAG laser operating at 354.7 nm with an average power of 12 W and a repetition rate of 30 Hz. At this excitation wavelength, the Stokes component of the Raman scattering occurs at 407.6 and 386.7 nm for water vapor and nitrogen, respectively. A 0.61-m telescope directs the collected light into the detection optics, where the beam is split into two channels that have different fields of view (FOV). The aperture of each channel is set to select a wide FOV of 2 mrad and a narrow FOV of 0.3

TABLE 1. Raman lidar specification.

Transmitter		Receiver	
Wavelength	355 nm	Diameter	61 cm
Laser	Nd:YAG third harmonic	Channel bandpass	0.4 nm
Energy/pulse	400 mJ	Filter transmission	30%–40%
Repetition rate	30 Hz	Field of view	Dual, adjustable (typically 0.3 mr, 2 mr)
Beam diameter	13 cm (~0.1 mr divergence)	Species	Rayleigh/aerosol (355 nm) Aerosol depol. (355 nm) Water vapor (408 nm) Nitrogen (387 nm)
Bandwidth	~2 cm^{-1}	Electronics	Photon counting 39-m range resolution

mrad. The wide FOV channels are better suited for profiling in the near field, as they admit more light (and background radiance) at these altitudes than the narrow FOV channels. After the field stops, the light is separated into the three wavelengths (elastic backscatter at the laser wavelength and the water vapor and nitrogen Raman signals) using dichroic mirrors and narrowband (0.4 nm) interference filters. This combination of the dual-FOV design and narrowband interference filters gives the CART Raman lidar excellent daytime capabilities without sacrificing its nighttime abilities. Table 1 lists some of the specifications of this system, and Fig. 1 provides a detailed layout of the receiver optics.

This Raman lidar system was designed to run autonomously: after the operator answers some preliminary questions and opens the hatch that protects the window on the telescope, no further operator action is required to operate the system. Automatically, the system proceeds to warm up the laser, adjusts the doubling and tripling crystals to maximize laser output power, and performs an alignment. It then collects several minutes of calibration data, which are used to help determine and monitor instrument characteristics such as system dead time and the overlap correction (described in section 3), before acquiring water vapor and aerosol data. Nominally, data are collected in 1-min intervals at the maximum 39-m resolution. However, during postprocessing, photons can be summed across many bins temporally or spatially, or both, to improve the signal-to-noise ratio. Periodically, the system pauses while collecting normal water vapor and aerosol data to maximize the power and optimize the alignment. The data are retrieved automatically from the lidar's computer by the CART site data system, by which the data are processed further to derive products, such as the water vapor mixing ratio, from the backscattered signals. Additional details can be found in Goldsmith et al. (1998).

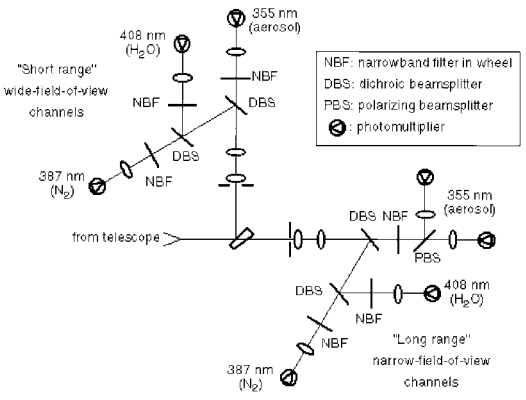

FIG. 1. Optical layout of the Raman lidar detection receiver.

3. Raman lidar calibration

Raman lidar systems detect selected species by measuring the wavelength-shifted molecular return produced by Raman scattering from the chosen molecules as a function of time since the laser's pulse. The ratio of the water vapor to the nitrogen return signals provides a profile that is nearly proportional to the water vapor mixing ratio [Eq. (2)]. To calibrate the mixing ratio profiles, one must first correct each signal to account for the characteristics of each channel, apply corrections to account for the detector's FOV and the differential atmospheric transmission between the two channels (Whiteman et al. 1992), and then multiply the ratio of the signals by a scale factor to convert it into absolute units.

The first step in the calibration is to characterize the system dead time for each channel. This correction accounts for the number of photons that are actually received by the lidar system that are uncounted. This occurs when two or more photons are counted as a single photon because they reach the photomultiplier tube too closely spaced in time to be distinguished as individual events. For this correction, we follow the technique outlined in Whiteman et al. (1992). The form of this correction is given in Eq. (3),

$$D(r) = \frac{R(r)}{1 + \tau R(r)}, \tag{3}$$

where D is the count rate of the detected signal, R is the ''real'' signal's count rate, r is the range, and τ is the dead-time parameter or the minimal amount of time needed between the arrival of two photons for them to be counted as individual events. The detected and real

signals are range dependent in Eq. (3), as the intensity of the backscatter drops according to the square of the range and, in addition, is dependent on the atmospheric density and other constituents. Note that the amount of correction increases with the detected count rate, and therefore, for small signals, the correction is negligible. The value of τ is determined for each channel by comparing full (nominal) and reduced strength data (i.e., data taken with an additional neutral density filter in the channel) collected during the lidar's calibration cycle. With sufficient attenuation, the reduced strength's signal can be assumed to be correct. Thus, the ''real'' signal is taken to be the reduced profile multiplied by the transmission of the neutral density filter. The value of τ can then be determined from these two datasets. After this constant is determined for a given channel, the count rate correction [Eq. (4), which is the inverse of Eq. (3)], which is solely a function of the detected count rate, is applied to all signals before further processing:

$$R(r) = \frac{D(r)}{1 - \tau D(r)}. \quad (4)$$

In practice, however, both the full and reduced strength signals are affected by the system dead time to some degree. Thus, the determination of the dead-time parameter τ and the transmission of the neutral density filter T_{nd} are found by minimizing Eq. (5) over the entire dynamic range of the signal

$$F(\tau, T_{\text{nd}}) = [R_f(r) - T_{\text{nd}}R_r(r)]^2 = \left[\frac{D_f(r)}{1 - \tau D_f(r)} - T_{\text{nd}}\frac{D_r(r)}{1 - \tau D_r(r)}\right]^2, \quad (5)$$

where D_f and D_r are the full and reduced strength-detected signals, respectively, and r is the range. The dynamic range of the signals has maximum count rate values that occur near 0.25 and 1.0 km for the WFOV and NFOV channels, respectively, and minimum values in the tail of the signals. The neutral density filter used here drops the signal by roughly one order of magnitude, and thus the value of T_{nd} is loosely constrained accordingly. Although the dead time for each channel is assumed usually to be stable—thus the abovementioned procedure should be used only once to determine the correction initially—this technique can be used to monitor the assumption of stability. Dead times for the different channels in this Raman lidar range from 4 to 8 ns.

As we use two different channels to measure simultaneously the Raman backscatter of both water vapor and nitrogen molecules, each channel may have a slightly different optical alignment that must be accounted for when creating the ratio of these two channels. This is the quantity $O(r)$ in Eq. (2). To derive this correction, we again follow Whiteman et al.'s (1992) example and replace all of the normal species-dependent interference filters in each channel with nitrogen interference filters. Then, by collecting Raman nitrogen-shifted data in all channels, the alignment differences between any two channels can be found by taking the ratio of the channels in this mode, since the two channels are measuring the same signal. If both channels were aligned perfectly and each channel had identical fields of view, this ratio would be constant with altitude. In practice, this correction is not constant with altitude, however, and is applied by dividing the ratio of the water vapor and nitrogen data by this resultant overlap correction. For the Raman lidar, the maximum correction for the water vapor mixing ratio is approximately 8% at 200 m and 15% at 600 m for the wide FOV (WFOV) and narrow FOV (NFOV) measurements, respectively. The maximum altitude at which this correction is applied is approximately 500 m for the WFOV mixing ratio profile and 5 km for the NFOV mixing ratio profile.

In addition to correcting for the differential overlap between the water vapor and nitrogen channels, a correction must be applied to the ratios that accounts for the differential atmospheric transmission between the two Raman wavelengths. This correction, $q(\lambda_{\text{wv}}, r)/q(\lambda_{\text{nit}}, r)$ in Eq. (2), is primarily due to the wavelength dependence of Rayleigh scattering. Hence, it increases with range away from the instrument and is approximately 7% at 10 km (Ferrare et al. 1995). Density profiles from *U.S. Standard Atmosphere, 1976* are used to account for this differential transmission, which allows this correction to be applied in real time. A correction for the differential transmission due to aerosol extinction at the two different wavelengths is not applied, as the correction is small (less than 3%–4%) for very hazy conditions (Ferrare et al. 1995), which seldom occur at the SGP CART site.

To summarize the processing steps up to this point, the first step is the correction for system dead time, which is applied to each channel individually. Using data collected before the laser is fired, the background level is determined, and this is subtracted from the received signal. The ratio of the water vapor and nitrogen signals is then performed, and the correction for the differential overlap $O(r)$ is applied. After applying the correction for the differential transmission, the result is proportional to the water vapor mixing ratio.

The final step in the calibration process is to derive the scalar, height-independent, calibration factor. This factor is derived from comparisons to other measurements of water vapor that can then be applied to the lidar's ratio profile. This eliminates the requirement to perform a precise radiometric calibration of the Raman lidar system, which can be very difficult because of uncertainties in the Raman cross sections and in determining the optical transmission characteristics of the lidar (Vaughan et al. 1988).

Raman lidar systems operate typically in the ultraviolet, since Raman scattering strength is inversely proportional to the fourth power of the excitation wavelength. The CART Raman lidar operates at 355 nm, the third harmonic of the Nd:YAG laser. Because of the

large solar background during daylight hours, however, the count rates can become large enough that the response of the photomultiplier tubes (PMTs), especially the 408-nm water vapor channels, becomes very nonlinear. The lidar, therefore, uses two operating modes: a *normal* mode for periods of low background radiance (such as nighttime periods), and a *bright* mode. The two modes differ only by the inclusion of an additional 10% neutral density filter in the water vapor channels when in bright mode, which attenuates the daytime signal sufficiently to keep the PMTs in a nearly linear regime. These two different modes must be calibrated individually.

At this point, four scalar calibration factors need to be determined, one for each of the narrow FOV (high) and wide FOV (low) channels, for both normal and bright mode. In an effort to keep the lidar data as self-consistent as possible, the low-channel calibration factors are derived to create the best fit with the high-channel ratios as possible over the altitude range in which both channels have adequate signal-to-noise ratios. For the nighttime data, this fit is performed between 1.3 and 1.6 km, which is beyond the maximum count rate, or peak, of the high channels' signals, which occurs at about 1 km. However, during the daytime, the increased background noise in the low (WFOV) channels prevents them from reaching this altitude. Therefore, the high and low channels are fit between 0.6 and 0.9 km. The importance of this calibration height difference will be discussed herein.

After relating the low to the high channels, only two calibration factors remain to be determined: the factor for the normal mode data and the factor for the bright mode. Traditionally, calibration factors for Raman lidar systems have been determined by fitting the lidar's profile to a set of coincident radiosonde profiles (Whiteman et al. 1992; Soden et al. 1994; Ferrare et al. 1995). However, recent analyses have shown significant sonde-to-sonde variability (Ferrare et al. 1995; Lesht and Liljegren 1996), as well as possible diurnal differences in the sonde calibrations (Soden et al. 1994; Turner et al. 1998). Hence, it was decided that a different instrument should be used for deriving the calibration factor for the Raman lidar. Microwave radiometers (MWRs), which measure the abundance of water vapor in the column, have proved to be very stable (Han et al. 1994). The MWR that has been at the SGP site for several years is well characterized (Liljegren and Lesht 1996) and was chosen as the calibration standard for the Raman lidar.

Normal-mode operation of the Raman lidar produces water vapor profiles that reach beyond 9 km and therefore sense more than 99% of the total precipitable water vapor (PWV) in the column at SGP. However, because of high background radiance during the daylight periods, the bright-mode profiles do not reach this altitude. Near solar noon, the average height reached by the lidar is around 3.5 km, which does not contain all of the PWV that is sensed by the MWR. To facilitate the lidar–

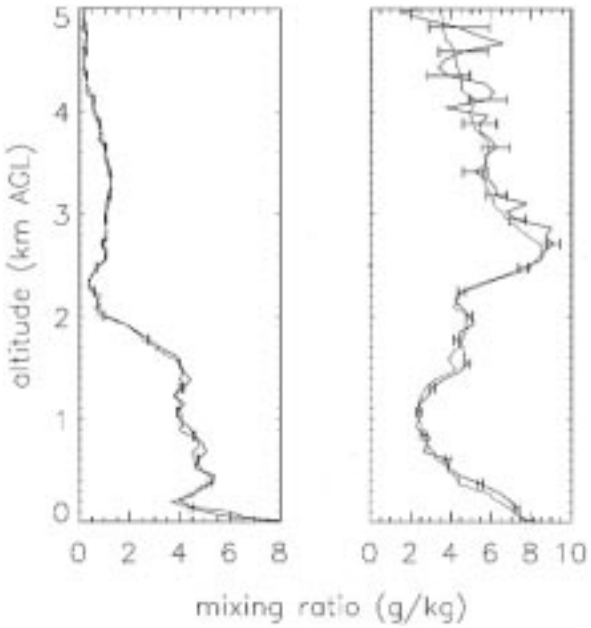

FIG. 2. Typical examples of water vapor mixing ratio profiles from the lidar (black, with error bars) and the radiosonde (gray) for both nighttime (left, 29 September 1997 at 0530 UTC, which is 0030 local) and daytime (right, 28 September 1997 at 1430 UTC, which is 0930 local). The lidar data were averaged for 10 min after the radiosonde's launch. The error bars on the lidar data were calculated using Poisson statistics for the observed photon counts.

microwave radiometer PWV comparisons, we estimate the fraction of the column sensed by the lidar by interpolating radiosonde profiles to the lidar sample time. From this interpolated profile, we calculate the amount of PWV below the maximum altitude of the lidar data for a given sample and then calculate the total PWV in the column. The ratio of these two values provides a unitless estimate of the fraction of the total column sensed by the lidar. This value is then used to scale the integrated column measured by the lidar, thus estimating the total column amount, which can then be compared directly to the MWR. For both of the water vapor IOPs, the lidar was typically measuring at least 80% of the total column amount of water vapor throughout the entire day.

We then calibrated both the normal and bright modes by comparing the PWV observed by the lidar (adjusted by the fraction indicated above) with the MWR. The calibration factors were obtained by minimizing the mean squared error between the two instruments' PWV for clear-sky cases in which the fraction of the column sensed by the lidar was 80% or greater. A single calibration value was used for each mode and for each IOP. Figure 2 shows an example demonstrating the excellent agreement between the water vapor mixing ratio profiles measured by the Raman lidar, which was calibrated to the MWR, and the coincident radiosondes during both nighttime and daytime. Because of the increased background radiance, the lidar's profiles extend to about 3.5–

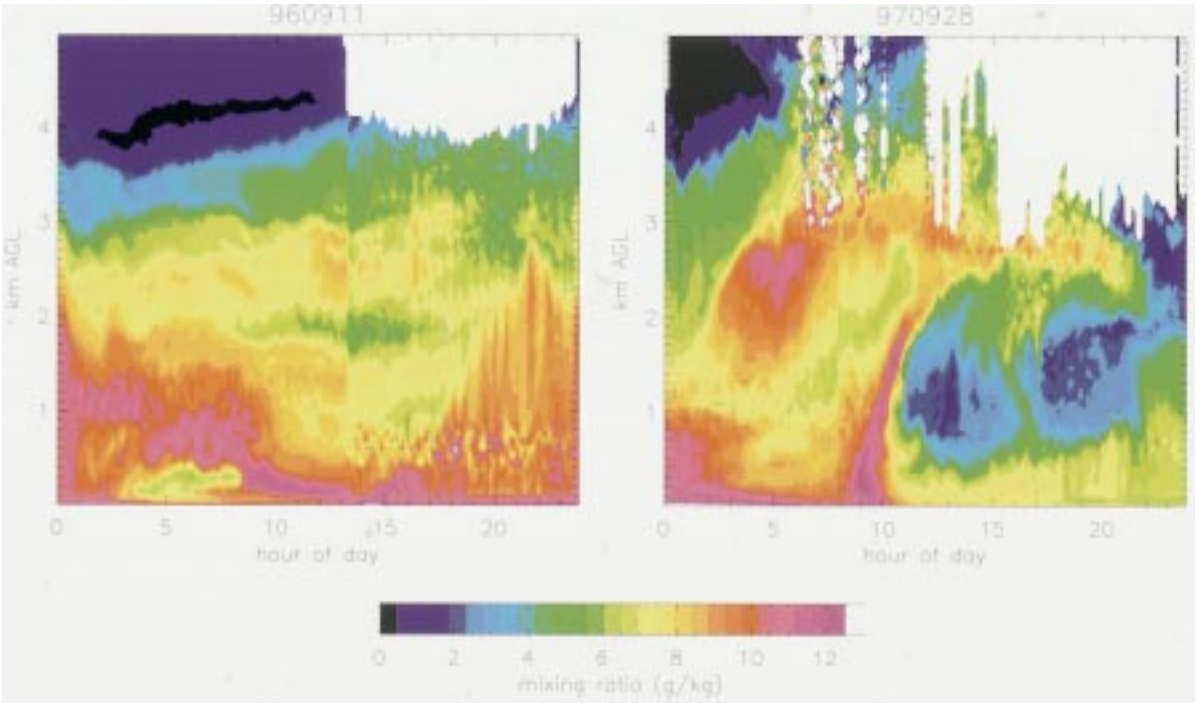

FIG. 3. Time–height cross sections of water vapor mixing ratio for 11 September 1996 (left) and 28 September 1997 (right). Note the calibration anomaly at shortly after sunrise (approximately 1300 UTC) on 11 September 1996, and the lack of it on 28 September 1997. The lidar data were averaged in 10-min intervals, with a vertical resolution of 78 m. (See text for explanation.)

4 km during the daytime (bright mode); however, the nighttime data (normal mode) extend beyond 10 km, with a signal-to-noise ratio of greater than 4 for averaging intervals of 10 min.

After completing the calibration steps described above, artificial ''transitions'' between the normal and bright modes could be seen in the time–height cross section images of mixing ratio data taken during the 1996 WVIOP (Fig. 3). Looking at the normalized differences in PWV during the IOP, such as in Fig. 4, a correlation between the background in the water vapor channels and the difference in PWV was noted. The

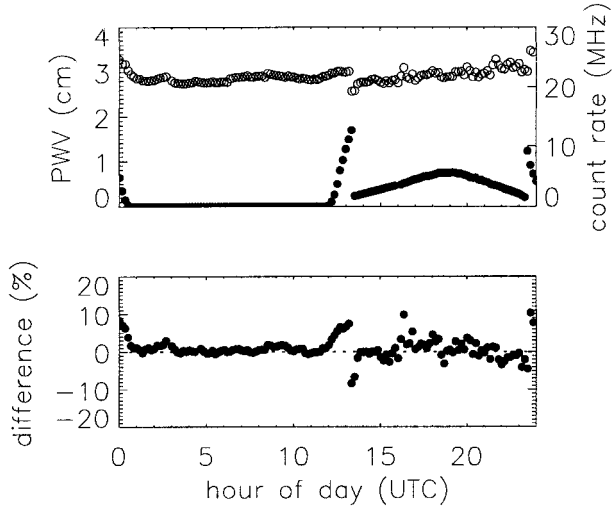

FIG. 4. (Upper) Total PWV measured by the Raman lidar (open circles, left axis) and the background count rate in the high water vapor channel (closed circles, right axis) on 11 September 1996. (Lower) The difference in PWV, calculated as $100(PWV_{lidar} - PWV_{MWR})/PWV_{MWR}$, as the lidar switches modes near sunrise or sunset correlates well with the background light levels in the water vapor channels. The background levels drop at approximately 1300 UTC and jumps up around 2330 UTC as the lidar transitions from normal to bright-mode and vice versa. The lidar data were averaged in 10-min intervals. This is a typical clear-sky example during the 1996 WVIOP.

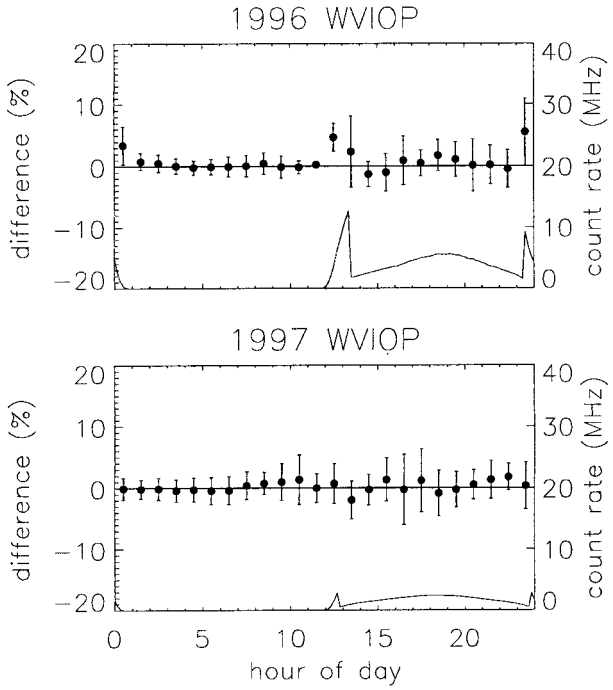

FIG. 5. Mean difference in PWV vs time of day (filled points, left axis) for the 1996 and 1997 WVIOPs. The error bars denote one standard deviation about the mean. Ten-minute lidar data were compared to similarly averaged MWR data, after which the results were collected into 0.5-h bins. Typical background levels from the high water vapor channel from each IOP are also plotted (right axis). Cloudy cases and cases where the lidar sensed less than 80% of the total column were excluded. Before the 1997 IOP, the lidar was modified to switch modes at lower background values to prevent the high count rate values in the water vapor channels during the sunrise or sunset periods.

inclusion of the additional neutral density filter in the water vapor channels when switching to bright mode shortly after sunrise [around 1300 UTC (0800 LDT)] drops the water vapor signal strength—and hence the background signal level—providing a feature in the background values that matches nicely with the PWV difference. Analysis of this phenomenon indicates that the water vapor channels seem to be experiencing an apparent count gain that acts as a function of the background light levels. A modification was made to the lidar's software configuration before the 1997 IOP that forced the transition between bright and normal modes when the background radiance is a factor of 4 lower. This modification improved greatly the water vapor images (Fig. 3) and the PWV statistics for the 1997 WVIOP in the sunrise or sunset periods when the lidar switches modes (Fig. 5). Currently, we are investigating the relationship between the background levels and the dead-time correction [Eq. (4)] to identify the physical cause of this phenomenon. One possibility is that the large continuous signal caused by the high background radiance may be causing a signal-induced gain change in the PMTs (Bristow et al. 1995). Since currently we do not have a correction for this error, we did not use the data from the sunrise or sunset periods of the 1996 WVIOP in the subsequent analyses.

4. Intercomparison results

a. Upper troposphere

The primary goal of the second WVIOP, which was held in September–October 1997, was the characterization of water vapor measurements in the upper troposphere. This regime is very important climatically, as errors in water vapor measurements at this altitude cause disproportionately large errors in calculating the net radiation escaping to space (Shine and Sinda 1991). To provide an additional water vapor measurement at these altitudes, in situ humidity data were collected by the University of North Dakota's Citation on several nights during the IOP.

To provide a baseline for the intercomparisons, the Raman lidar profiles were compared to the radiosondes launched less than 80 m from the lidar's enclosure during both IOPs. For this analysis, the lidar data were averaged for 30 min after the radiosonde's launch, and the vertical resolution at these altitudes was decreased to 156 m up to 9.5 km and 312 m above 9.5 km from its maximum resolution of 39 m. Lidar data were used only if signal-to-noise was greater than 4. As part of another experiment occurring during both IOPs, several of the balloons were launched with two radiosonde packages taped together, to gather statistics on the sonde-to-sonde variability.

After identifying (using the aerosol scattering ratio data derived from the Raman lidar) and removing the cloudy cases, the normalized difference profiles were calculated for each lidar–sonde pair. The mean of these difference profiles, each computed as $100.0(w_{\text{lidar}} - w_{\text{sonde}})/w_{\text{lidar}}$, is shown in Fig. 6 for both the nighttime (normal mode) and daytime (bright mode) data. The error bars in this figure denote the standard deviation of the mean difference. The differences between the mean difference profiles from the two IOPs are negligible. Figure 7 concentrates on the upper-tropospheric measurements made at night, illustrating both the mean normalized difference and the mean bias between the lidar and the radiosondes. The difference between the two measurement techniques is a bias of less than 0.05 g kg^{-1} from 6 to 11 km, which results in a relatively small error as a normalized difference at 6 km, but a large (greater than 25%) error at 11 km.

The North Dakota Citation flew three different types of hygrometers during the 1997 WVIOP: a cryogenic frost-point hygrometer from Buck Research (Bussen and Buck 1995), an EG&G dewpoint hygrometer, and a LiCor dewpoint hygrometer (LI-COR, Inc. 1990). The LiCor hygrometer was unable to provide measurements in the low temperature regime above 8 km, and hence we concentrated on the other two hygrometers. Prob-

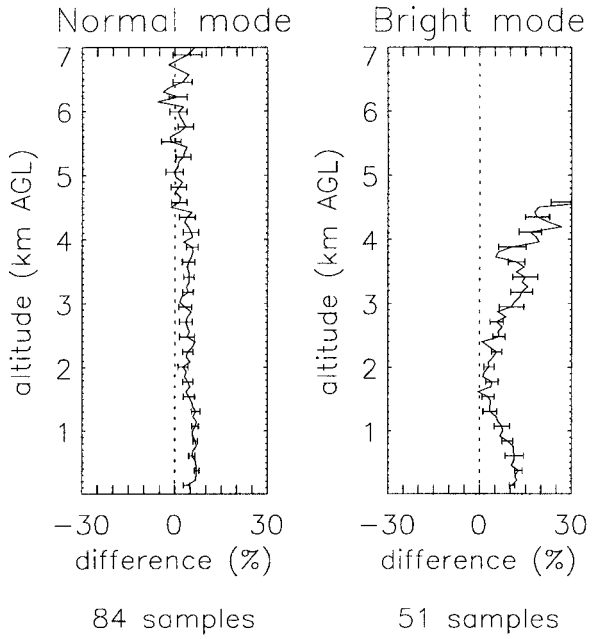

FIG. 6. Mean difference profile in mixing ratio, calculated as $100(w_{\text{lidar}} - w_{\text{sonde}})/w_{\text{lidar}}$, for data from both IOPs. The error bars denote one standard deviation of the mean difference. The lidar data were averaged for 30 min after the launch of the radiosondes. Lidar data with a signal-to-noise ratio less than 4 at a given altitude were not used, nor were data above the cloud base. Normal mode is the lidar's nighttime mode; bright mode is used during the day. (See text for details.)

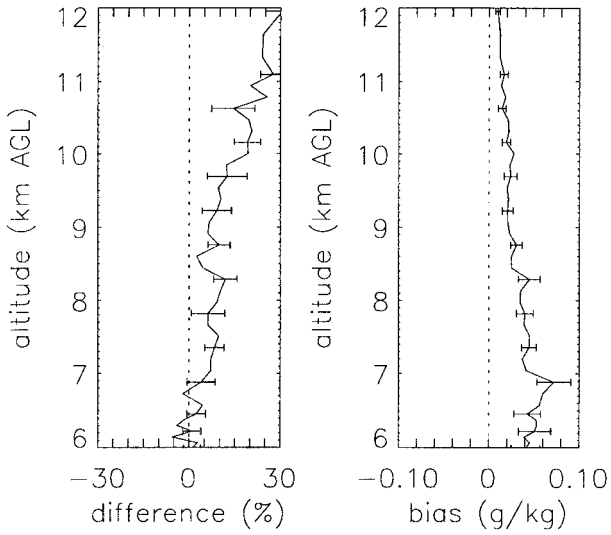

FIG. 7. Nighttime upper-tropospheric differences between the Raman lidar and radiosondes, both in terms of normalized differences and bias. The error bars denote one standard deviation of the mean.

lems with the EG&G and cryogenic instruments precluded use of the data from two of the high-altitude nighttime missions, so only the flights from 26 September, 30 September, 1 October, and 4 October provide useful data when the lidar was operating. Time–height cross sections of water vapor mixing ratio data from the lidar indicate that in the latter three cases the upper troposphere was fairly stationary when the Citation was in the air, allowing the lidar's data to be averaged for 3 h to improve the signal-to-noise ratio. These case studies are shown in Fig. 8. These flights were coor-

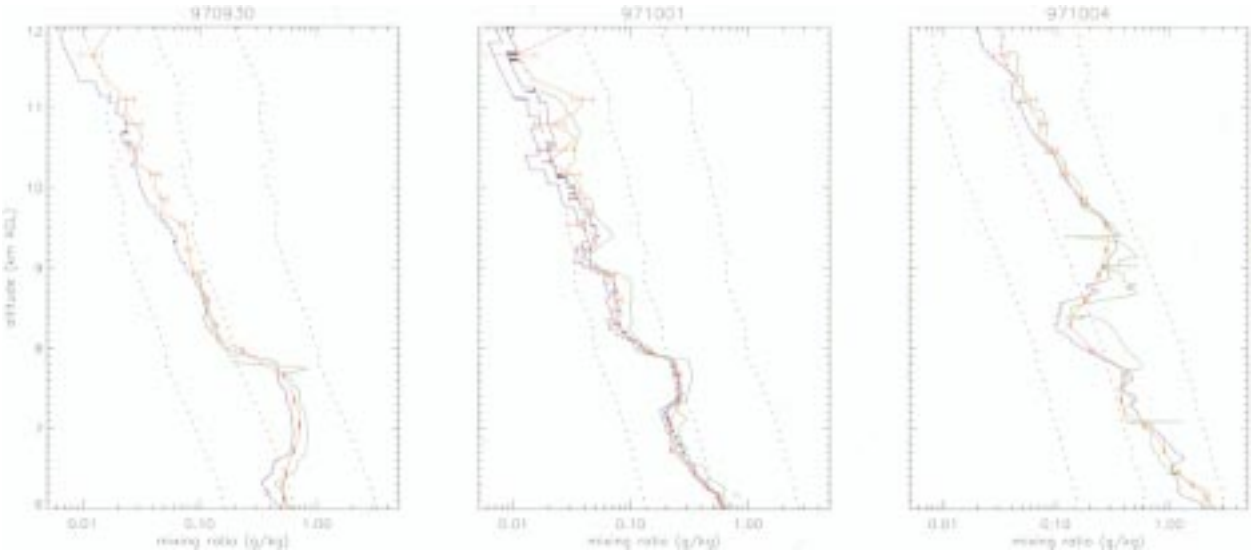

FIG. 8. Upper-troposphere case studies during the 1997 WVIOP, comparing the lidar (red), radiosondes (blue), and the North Dakota Citation's hygrometers (green). The dotted lines represent 5%, 20%, and 100% relative humidity. Lidar data were averaged to 156-m resolution up to 9.5 km, and 312-m resolution above 9.5 km, with 3-h temporal resolution. The balloon on 1 October carried two radiosonde packages. (See text for details.)

dinated such that a radiosonde was launched and was at approximately the same altitude as the Citation when it neared the top of its profile.

The Citation's frost-point hygrometer did not function on 30 September, but the EG&G hygrometer made good measurements up to 9 km and agreed quite well with the lidar between 8 and 9 km. The radiosonde began diverging from the lidar quite low (around 6 km), running about 20% drier than the lidar between 6 and 11 km, above which the difference between the two increased. The balloon launch on 1 October included two radiosonde packages, thus providing two comparisons with the Citation flight this evening. The frost-point hygrometer malfunctioned on the ascent but gave a complete descent profile. The EG&G device had problems on this flight above 7 km and is excluded from the plot. One radiosonde agrees very well with the lidar up to 10 km, but the other sonde package started disagreeing with the lidar at 7.5 km, with the difference between the two ranging from 10% at 8 km to 20% at 10 km. Above 10 km, both radiosondes diverged rather quickly from the Raman lidar. The frost-point data from the Citation maintained a constant 20% moist bias with respect to the lidar from 6 km to approximately 10.5 km. The final flight of the IOP was on 4 October, the most moist of the three nights. During the aircraft's ascent, both of the hygrometers had difficulties; however, the EG&G hygrometer provided quality data between 9.5 and 12 km. The EG&G data agree within 10% of the lidar data over this range. The agreement between the lidar and the radiosonde this night is excellent at 10 km, but the difference between the two grew rapidly to almost 20% at 11 km. The measurements from the frost-point hygrometer were valid only on the descent below 9 km and are excluded from the plot.

Signal-induced noise, or afterpulsing, can become a significant fraction of the detected signal at high altitudes and would tend to moisten the lidar data in our application. However, Bisson et al. (1994) have shown that by increasing the signal in the water vapor channel (by directing more light into it, for instance) and by selecting PMTs with low background count rates, water vapor profiles approaching the tropopause can be retrieved. Since the modeling and extraction of the signal-induced noise component can be fraught with difficulties (Ferrare et al. 1995), PMTs with low afterpulsing characteristics as well as low background noise levels were selected for this instrument (Goldsmith et al. 1998). This, combined with the fact that the differences with the Citation data between 9 and 11 km on 1 and 4 October seem independent of altitude, suggests that signal-induced noise is not a problem in the lidar data at these altitudes.

The mean difference profile between the Raman lidar and the Vaisala radiosondes suggest that the radiosondes are 10%–30% drier than the lidar between 10 and 12 km, which is similar to results from both Soden et al. (1994) and Ferrare et al. (1995). However, this bias could also be attributed to a small amount of signal-induced noise in the lidar measurements. Analysis of the Citation data in these case studies suggests that perhaps both the lidar and the radiosonde are dry in the upper troposphere, and it indicates that the observations of upper-tropospheric moisture must continue to be the focus in the near future.

b. Daytime measurements

Raman lidar measurements of water vapor during the daytime are much more difficult due to the relatively weak Raman backscattered signal and the presence of high solar background levels. The CART Raman lidar is able to make these daytime measurements by using narrowband interference filters together with a narrow FOV. This approach helps to eliminate a large portion of the background solar noise by receiving only the specific wavelengths of interest from the direction of interest and thus keeps the signal-to-noise reasonable. Nonetheless, the amplitude of the daytime background is such that the lidar's profile is limited to about 3.5 to 4 km during the day. Figures 9 and 10 show time–height cross sections of water vapor mixing ratio for two 4-day periods from each IOP, which demonstrates the remarkable variability of water vapor in the atmosphere. The regions in which the signal in the water vapor channel reaches the background level (and hence the signal-to-noise ratio becomes unity) are indicated in the image by the areas that are whited out. It should be noted that the variations in the maximum altitude that can be profiled during the day (as well as the night) are a function of the amount of temporal and vertical averaging as well as of the system power and the amount of water vapor present, the last of these being the most important (Ferrare et al. 1995). The data in these images were averaged for 10 min, with a vertical resolution of 78 m.

An obvious feature of the 1996 data (Fig. 9) is the occurrence of artificial discontinuities in the images during the lidar's transition times near sunrise or sunset. As indicated in section 3, the simple modification made to the system that causes the lidar to switch between the two modes when the background value is lower essentially solves this problem. This improvement is clear in the 1997 water vapor image (Fig. 10). Analysis of the 1997 precipitable water vapor data during the transition times indicates that some differences still exist between the lidar and the microwave radiometer when the background is changing rapidly, but these errors are within 2%–3%.

The solar background during the day affects the low channels more than the high channels because the former have a wider FOV, and thus more background light is directed to the low channel PMTs. This reduces the range of the low-channel profiles by masking the weak Raman signal, which forces the high and low channels to be merged closer to the surface during the day than at night, as discussed in section 3. Since the count rate

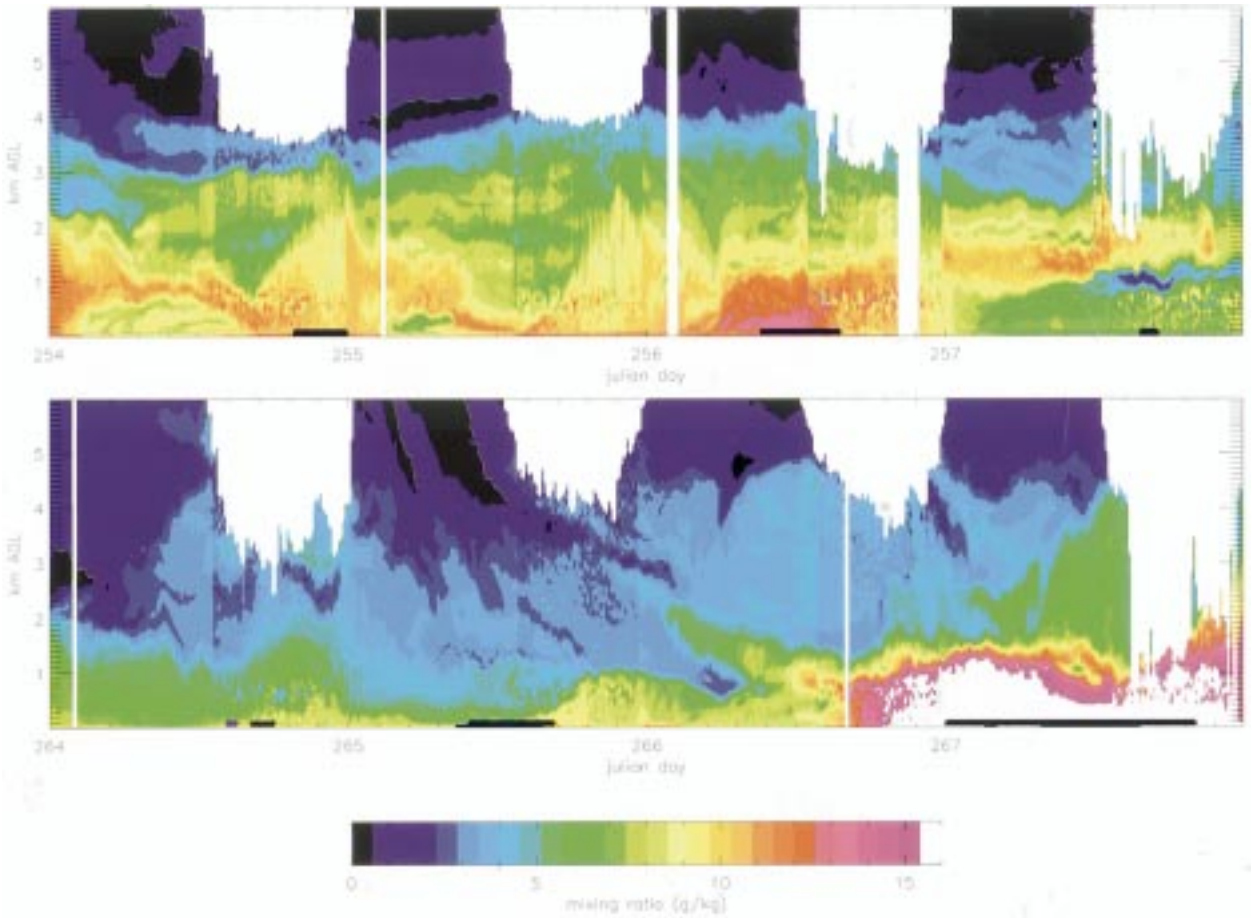

FIG. 9. Time–height cross sections of water vapor mixing ratio for two 4-day periods during the 1996 WVIOP. The whited out areas above 3 km during the day denote the maximum range the lidar can sense during the day. Black stripes at the bottom of the images denote missing data from the instrumented tower, which is used to extend the lidar measurements to the surface. The smaller vertical white gaps are calibration cycles, while the larger gaps denote periods when the lidar was down (either for modification, experimentation, or mechanical issues). Sunset occurs approximately at the beginning of the Julian day.

correction [Eq. (4)] is largest at the peak of the signal, which occurs at approximately 1 km in the high-channel data, small errors in this correction [because of either the determination of the dead-time parameter τ in Eq. (4) or the assumption of the correction's functional form] could translate into errors in the daytime around 1 km and thus more greatly affect the calibration of the low-channel bright-mode data.

The bright-mode statistics in Fig. 6 illustrate the daytime mean difference between the lidar's mixing ratio profiles and radiosondes, where the statistic was computed as $100.0(w_{\text{lidar}} - w_{\text{sonde}})/w_{\text{lidar}}$ for each altitude bin. The mean difference is less than 3% between 1.2 and 3 km, but this increases to about 9% from the surface to 1 km, with the lidar being, in general, wetter than the radiosondes in this regime. Daytime in situ profiles from the Pacific Northwest National Laboratory Gulfstream aircraft were acquired near solar noon (approximately 1800 UTC, or 1300 local time) during the 1997 WVIOP (Fig. 11). Comparisons with these profiles also indicate that the lidar may be slightly moister in the lowest kilometer, although the overall agreement is excellent. The nighttime residuals suggest a similar feature, although the magnitude of the residuals between the lidar and the sondes in this region are smaller at night than during the day. This change in the size of the residuals suggests the possibility that the sondes have a diurnal feature that affects their near-surface measurements [diurnal differences in radiosondes have been suggested by Soden et al. (1994) and Turner et al. (1998)]. However, another possible explanation is that the change in solar background levels of more than four orders of magnitude affects the detection electronics of the lidar system subtly, and research in this area continues.

These differences between the Raman lidar and other measurements are small and remain relatively constant with time, both of which make the data collected by the lidar useful for atmospheric studies. The comparisons to the MWR (Fig. 5) from both IOPs show that the

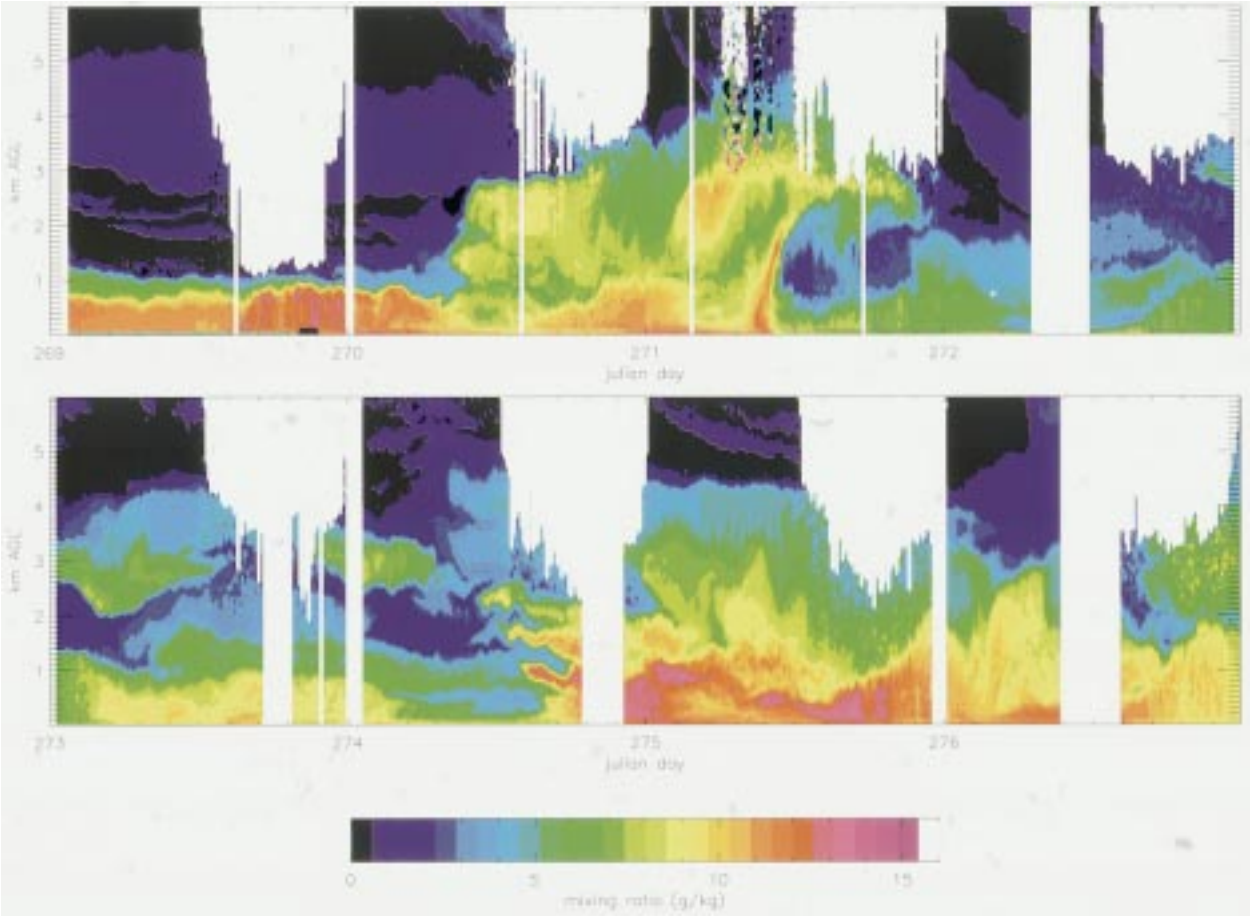

FIG. 10. Time–height cross sections for two 4-day periods during the 1997 WVIOP. A communication problem with the filter wheel controller, which automatically rotates different filters into and out of the channels, caused the lidar to stop collecting data occasionally.

variation between the MWR and the lidar increases slightly during the day. However, given the large increase in the background noise during the day, the slight increase in the spread is expected. Furthermore, the relative sizes of these error bars provides evidence of the stability of both the lidar and the MWR.

c. Lowest kilometer

There is an instrumented 60-m tower at the SGP CART site that provides in situ measurements of temperature and relative humidity at heights of 25 and 60 m using Vaisala HMP35D sensors. Although mixing ratio values can be derived from the CART Raman lidar at 60 m, data at these low altitudes are very sensitive to errors in the determination of the overlap correction (section 3), and the signal-to-noise ratio is much smaller. Concerns about the range-dependent ray angle before the 1996 WVIOP resulted in interference filters, with a bandpass of 1.2 nm being used in the wide FOV channels. However, sequential comparisons with interference filters having a bandpass of 0.4 nm during the IOP showed no evidence of ray angle range dependence. Hence these narrower band filters replaced the originals before the 1997 WVIOP (Goldsmith et al. 1998).

Figure 12 shows some comparisons at the 60-m level from the instrumented tower and the appropriate bin from the lidar's wide FOV channel for the 1997 WVIOP. These results are very similar to the 1996 results, with the exception that the scatter in the daytime measurements has been reduced greatly by using the 0.4-nm bandpass interference filters. The normal-mode results show excellent agreement, on average, with a mean difference computed as $100.0(w_{\text{lidar}} - w_{\text{tower}})/w_{\text{tower}}$, of 1.9% and a standard deviation about the mean of 4.9%. The daytime results are somewhat worse, with a mean difference of 7.1% and a standard deviation about the mean of 8.9%. However, given the relatively low signal to noise at this altitude, the results are quite impressive. Furthermore, the normalized differences for both modes are consistent with time, as the number of samples in Fig. 12 spans a continuous 10-day period, again demonstrating the stability of the Raman lidar.

During both IOPs, chilled mirror hygrometers (Meteor AG) were flown on the Los Alamos National Laboratory tethersonde when the winds were below 10 m

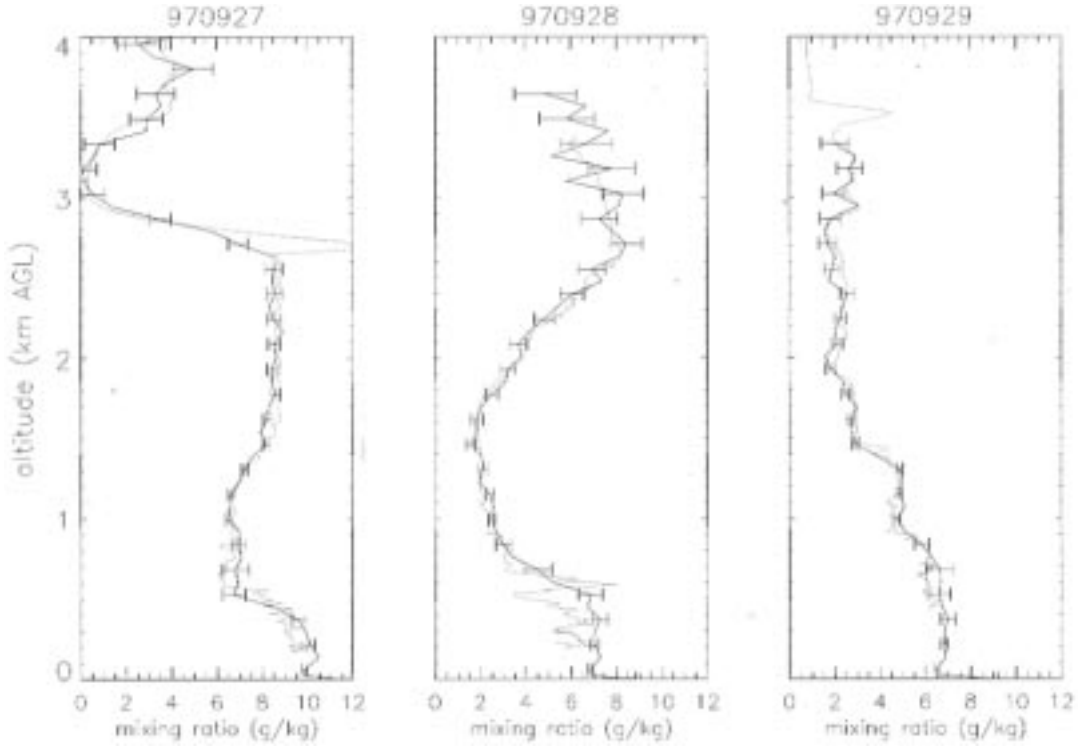

FIG. 11. Daytime mixing ratio profiles measured by the Raman lidar (black, with error bars) and the PNNL Gulfstream (gray) during the 1997 WVIOP. These descending profiles occurred at approximately 1700 UTC on 27 September, 1830 UTC on 28 September, and 2000 UTC on 29 September. Lidar data were averaged for 10 min to correspond with the descent of the Gulfstream. The large spike seen in the Gulfstream data on 27 September at 2.7 km is aphysical.

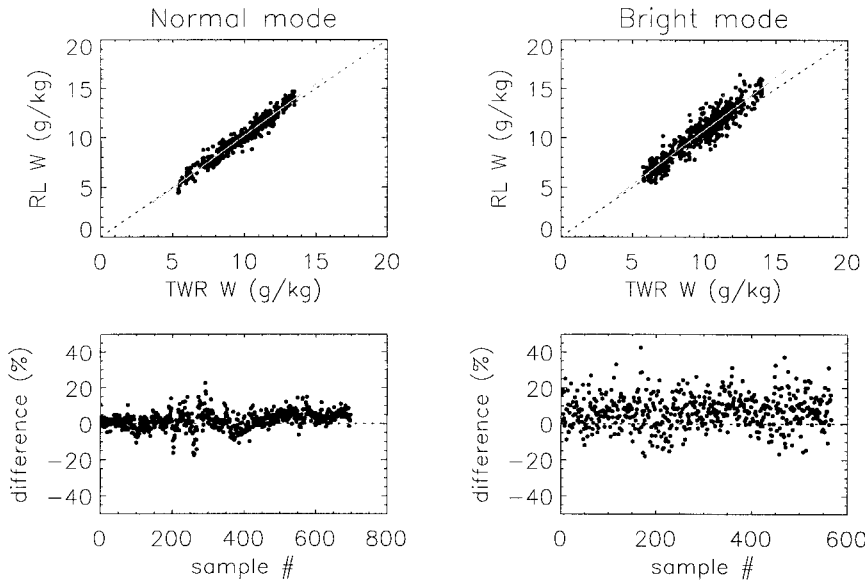

FIG. 12. Comparisons at the 60-m level between the instrumented tower and the lidar's low channel during the 1997 WVIOP. The upper plots are scatterplots of mixing ratio between the two measurements, segregated into normal- and bright-mode measurements. The lower plots show the normalized difference, computed as $100(w_{\text{lidar}} - w_{\text{tower}})/w_{\text{tower}}$, between the two systems for the samples taken during the IOP. Both datasets are 10-min averages and span 10 consecutive days. The larger scatter in the bright-mode data is due to the increased amount of solar background noise during the daytime.

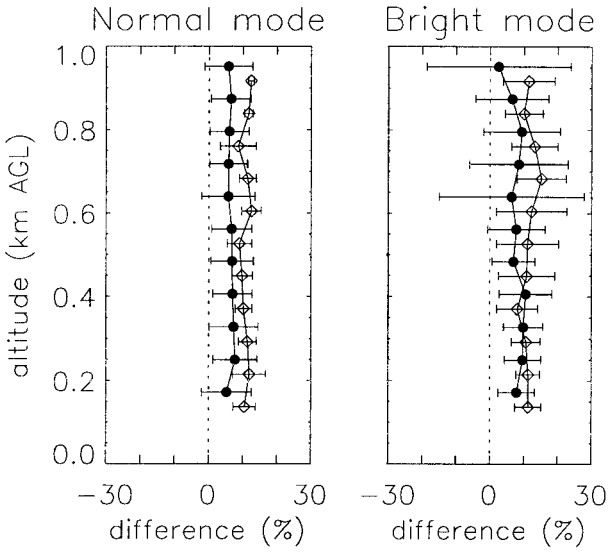

FIG. 13. Mean difference profiles in mixing ratio between the lidar and the radiosondes (filled circles) and chilled mirror hygrometers flown on the tethersonde and kite (open triangles) during the 1996 WVIOP. The radiosonde statistics are offset by 30 m for clarity. The mean difference was computed as $100(w_{\text{lidar}} - w_{\text{other}})/w_{\text{lidar}}$. There were 69 radiosondes and 13 chilled mirror flights in the normal-mode statistics. There were 33 radiosondes and 32 chilled mirror flights in the bright mode.

s^{-1}, or on the University of Colorado kite system when the winds were between 8 and 15 m s^{-1}, to provide additional profiles of water vapor in the lowest kilometer. The chilled mirror measurements from both platforms will be referred to as tethersonde measurements in this paper. Since these lowest levels are the most sensitive to the overlap correction, the addition of tethersonde, as well as the standard radiosondes, can be used to identify any discrepancies in this correction. The outgoing laser beam is totally within the low-channel FOV (i.e., the overlap correction is unity) at approximately 500 m, while the high-channel overlap function extends almost to 5 km. Therefore, since the tethersonde was restricted to a maximum altitude of less than 1 km by the Federal Aviation Administration during these IOPs, only the low-channel overlap correction can be validated completely. Because the FOV of the system does not change diurnally, the same overlap correction is used for both the normal- and bright-mode data.

The mean difference between the lidar and the tethersondes for both nighttime and daytime flights during the 1996 WVIOP are shown in Fig. 13. The difference is calculated as $100.0(w_{\text{lidar}} - w_{\text{other}})/w_{\text{lidar}}$, where "other" is either the radiosonde or the chilled mirror measurements from the tethersonde. The error bars represent the standard deviation about the mean difference at each altitude level. Since the merge region for the normal-mode data is from 1.3 to 1.6 km, the residuals shown for the nighttime data are for the lidar's low channel only. From this plot, the constant residuals indicate that the overlap function has been determined very well, with the possible exception at the 135-m level. The overlap correction decreases monotonically beyond the count rate peak of the signal (for the low channels, this is approximately 200 m), and hence, the feature in the tethersonde residuals near 600 m is probably due to spatial sampling issues.

Comparing the nighttime residuals with the daytime residuals reveals two important features. First, the larger error bars between 500 and 800 m in the day were expected, as this is near the end of the maximum usable range for the low channels, and it is in this range that we are changing linearly to the high-channel data. However, below 500 m, the mean difference between the Raman lidar and the sondes has increased by about 4% from night to day, while the mean difference between the lidar and the chilled mirrors on the tethersonde has remained virtually unchanged. Since the lidar–tethersonde residuals seemed to have remained constant for both night and day, the change in the residuals between the lidar and the radiosondes is more likely attributable to the radiosonde measurements. Comparisons against the chilled mirror hygrometers flown on the tethersonde during the 1997 WVIOP show very similar results. This provides further evidence of a possible diurnal feature in radiosonde performance, which was shown earlier in the change in the mean difference profiles between the lidar and sonde below 1.5 km in Fig. 6.

5. Future work

Determining the dead-time correction, the first correction applied to the data, is critical for calibrating this instrument. The correction used here [Eq. (3)] assumes that the detection electronics are *nonparalyzable*. That is, as the real signal increases, the detected signal continues to rise, eventually achieving some maximum, where it remains fixed as the real count rate continues to increase. Another model is the *paralyzable* correction, in which the detected signal rises as the real signal does until the real signal reaches some point, after which the detection electronics become saturated and actually start recording less signal. The functional form for the latter correction is

$$D(r) = R(r) \exp[-\tau R(r)], \tag{6}$$

and a comparison of the two corrections is given in Fig. 14. Typically, tests are performed to determine the characteristics of the detection electronics by gradually increasing the amount of light reaching a channel until it saturates, since its response dictates which correction to use to account for the dead time of that channel.

For low count rates, there is little difference between the two corrections aside from the ease of implementation. Since Eq. (3) has a closed-form inverse [Eq. (4)], the real signal can be computed directly from the detected signal. However, approximations are needed to calculate the real signal from the detected signal in Eq. (6). Also, since the inverse of the paralyzable correction

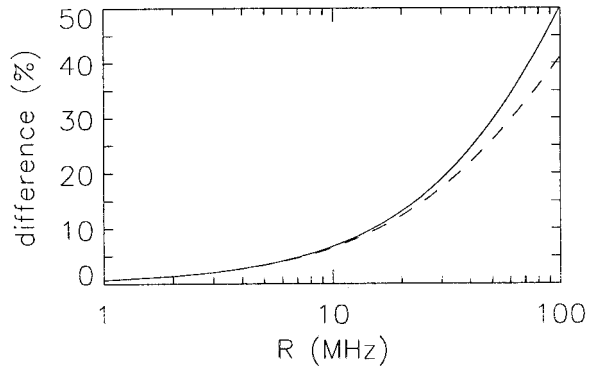

FIG. 14. Size of the nonparalyzable [Eq. (3), dashed line] and the paralyzable [Eq. (6), solid line] corrections as a function of the real signal, using a typical dead time of 7 ns.

is not a single-valued function, there is some uncertainty in deciding which value to use for a given $D(r)$, especially if $D(r)$ is near its maximum.

Careful consideration has been given to the design of the receiving optics of the Raman lidar to keep the count rates for each channel in the near-linear operating regime of the PMTs. However, because of the requirement to profile both in the near field and in the upper troposphere, signal strengths can vary in each of the channels as much as four orders of magnitude throughout the profile. Furthermore, the variable nature of the atmosphere can cause the signals to vary greatly over time at each altitude bin. This variability presents a difficult challenge when optimizing the amount of light directed to each PMT.

Based on nominal maximum count rates for each channel (20 MHz) and the observed dead time of the Raman lidar electronics (7 ns), the difference in the correction between the nonparalyzable and paralyzable assumptions is less than 5%. Hence, the decision was made to use the former correction because of its implementation ease. However, some of the data taken during these IOPs have large count rates beyond this nominal count rate, where there are significant differences between the two correction algorithms. More tests need to be conducted on the Raman lidar's PMTs and detection electronics to determine which of the corrections is more appropriate, or to directly model a different correction if neither of the two approximations above fits the data well. This future work may demonstrate some inadequacies at the highest count rates and provide a method to correct the detected signal in these cases, possibly improving the data at the peak of the high channel during the daytime and/or the sunrise or sunset periods.

6. Conclusions

The CART Raman lidar was designed to provide excellent daytime water vapor measurements without sacrificing its nighttime abilities and thus allowing the lidar to make high-resolution measurements that span the diurnal cycle. The continuous measurements by this Raman lidar render it invaluable for studying variability of the water vapor in the atmosphere. Synoptic events, such as the cold fronts on Julian day 256 in 1996 (Fig. 9) and Julian day 271 in 1997 (Fig. 2 and Fig. 10), were captured in detail by the high temporal and vertical resolution of the lidar, providing a wealth of data such as in earlier analyses (Melfi et al. 1989). Researchers can use these data to study the evolution of the water vapor fields in the boundary layer throughout the diurnal cycle (Melfi and Whiteman 1985). For those who are performing detailed model evaluations, such as line-by-line radiative transfer models, the high temporal resolution of the lidar can be used to identify stationary periods as a function of altitude, for which averaging may be beneficial. The Raman lidar has also demonstrated its ability to profile water vapor in the upper troposphere, and its temporal coverage makes it a natural choice to use for validation of remotely sensed profiles from spacecraft.

The primary goal of this paper was to evaluate the Raman lidar, which was delivered to the site before the first water vapor IOP. Comparisons of the lidar data with the microwave radiometer for both IOPs have shown that the nighttime differences in total precipitable water vapor are within 3%, on average, which increase slightly during the day because of the noisier background conditions. Similarly, point comparisons at 60 m with the instrumented tower also demonstrate similar accuracy. In addition, the time series differences indicate the stability of this instrument to make these measurements for weeks at a time. The comparisons of the vertical profiles of water vapor mixing ratio are excellent with both the radiosondes and the humidity measurements from the aircraft. This analysis has also indicated that the Vaisala radiosondes may be 10%–30% dry in the upper troposphere, or that the lidar data are affected by a small amount of signal-induced noise. Furthermore, comparisons of the lidar data with the chilled mirror profiles flown on the tethersonde and kite systems and radiosondes suggest that there is a diurnal characteristic that affects the radiosondes in the lowest kilometer.

The addition of this Raman lidar has greatly improved the water vapor measurement capabilities at the ARM CART site. These results have highlighted the lidar's abilities, demonstrating the accuracy of its measurements and the stability to make them over time. Some concerns and direction for future work have also been discussed.

More information about the ARM project, as well as data from the Raman lidar and other instruments at the CART site, can be found on the ARM Web site at http://www.arm.gov.

Acknowledgments. We would like to thank Rich Ferrare and Dave Whiteman for several fruitful discussions

on this work. This work was funded by the U.S. Department of Energy (DOE) Atmospheric Radiation Measurement program. Pacific Northwest National Laboratory is operated for the U.S. DOE by Battelle under Contract DE-AC06-76RLO-1830. Sandia National Laboratories is a multiprogram laboratory operated by Sandia Corporation, a Lockheed Martin company, for the U.S. DOE under Contract DE-AC04-94AL8500.

REFERENCES

Bisson, S. E., J. E. M. Goldsmith, and A. D. Del Genio, 1994: Measurements of upper tropospheric moisture with a Raman lidar. *17th Int. Laser Radar Conf.,* Sendai, Japan, International Radiation Commission, 134–136.

Bristow, M. B., D. H. Bundy, and A. G. Wright, 1995: Signal linearity, gain stability, and gating in photomultipliers: Applications to differential absorption lidars. *Appl. Opt.,* **34,** 4437–4452.

Bussen, R., and A. Buck, 1990: A high-performance hygrometer for aircraft use: Description, installation, and flight data. *J. Atmos. Oceanic Technol.,* **12,** 73–84.

Cooney, J. A., 1970: Remote measurements of atmospheric water vapor profiles using the Raman component of laser backscatter. *J. Appl. Meteor.,* **9,** 182–184.

Donovan, D. P., J. A. Whiteway, and A. I. Caswell, 1993: Correction for nonlinear photon-counting effects in lidar systems. *Appl. Opt.,* **32,** 6742–6753.

Ferrare, R. A., S. H. Melfi, D. N. Whiteman, and K. D. Evans, 1992: Raman lidar measurements of Pinatubo aerosols over southeastern Kansas during November–December 1991. *Geophys. Res. Lett.,* **19,** 1599–1602.

——, S. H. Melfi, D. N. Whiteman, K. D. Evans, F. J. Schmidlin, and D. O'C. Starr, 1995: A comparison of water vapor measurements made by Raman lidar and radiosondes. *J. Atmos. Oceanic Technol.,* **12,** 1177–1195.

Goldsmith, J. E. M., F. H. Blair, S. E. Bisson, and D. D. Turner, 1998: Turn-Key Raman lidar for profiling atmospheric water vapor, clouds, and aerosols. *Appl. Opt.,* **37,** 4979–4990.

Han, Y., J. B. Snider, E. R. Westwater, S. H. Melfi, and R. A. Ferrare, 1994: Observations of water vapor by ground-based microwave radiometers and Raman lidar. *J. Geophys. Res.,* **99,** 18 695–18 702.

Lesht, B. M., and J. C. Liljegren, 1996: Comparison of precipitable water vapor measurements obtained by microwave radiometry and radiosondes at the Southern Great Plains CART site. *Proc. Sixth Atmospheric Radiation Measurement (ARM) Science Team Meeting,* San Antonio, TX, U.S. Department of Energy, 165–168.

LI-COR, Inc., 1990: LI-6262 CO_2/H_2O Analyzer operating and service manual. Publication No. 9003-59, 84 pp. [Available from LI-COR, Inc., P.O. Box 4425, 4421 Superior Street, Lincoln, NE 68504.]

Liljegren, J. C., and B. M. Lesht, 1996: Measurements of integrated water vapor and cloud liquid water from microwave radiometers at the DOE ARM cloud and radiation testbed in the U.S. southern Great Plains. *Proc. Int. Geoscience and Remote Sensing Symp. (IGARSS),* Lincoln, NE, IEEE, 1675–1671.

Measures, R. M., 1984: *Laser Remote Sensing: Fundamentals and Applications.* Wiley.

Melfi, S. H., and D. N. Whiteman, 1985: Observation of lower-atmospheric moisture structure and its evolution using a Raman lidar. *Bull. Amer. Meteor. Soc.,* **66,** 1288–1292.

——, J. D. Lawrence Jr., and M. P. McCormick, 1969: Observation of Raman scattering by water vapor in the atmosphere. *Appl. Phys. Lett.,* **15,** 295–297.

——, D. Whiteman, and R. Ferrare, 1989: Observation of atmospheric fronts using Raman lidar moisture measurements. *J. Appl. Meteor.,* **28,** 789–806.

Shine, K. P., and A. Sinda, 1991: Sensitivity of the earth's climate to height-dependent changes in water vapor mixing ratio. *Nature,* **354,** 382–384.

Soden, B. J., S. A. Ackerman, D. O'C. Starr, S. H. Melfi, and R. A. Ferrare, 1994: Comparison of upper tropospheric water vapor from GOES, Raman lidar, and cross-chain loran atmospheric sounding system measurements. *J. Geophys. Res.,* **99,** 21 005–21 016.

Stokes, G. M., and S. E. Schwartz, 1994: The Atmospheric Radiation Measurement (ARM) program: Programmatic background and design of the cloud and radiation testbed. *Bull. Amer. Meteor. Soc.,* **75,** 1201–1221.

Turner, D. D., T. R. Shippert, P. D. Brown, S. A. Clough, R. O. Knuteson, H. E. Revercomb, and W. L. Smith, 1998: Long-term analysis of observed and line-by-line calculations of longwave surface spectral radiance and the effect of scaling the water vapor profiles. *Proc. Eighth Atmospheric Radiation Measurement (ARM) Science Team Meeting,* Tucson, AZ, U.S. Department of Energy, 773–776.

Vaughan, G., D. P. Waring, L. Thomas, and V. Mitev, 1988: Humidity measurements in the free troposphere using Raman backscatter. *Quart. J. Roy. Meteor. Soc.,* **114,** 1471–1484.

Whiteman, D. N., S. H. Melfi, and R. A. Ferrare, 1992: Raman lidar system for the measurement of water vapor and aerosols in the Earth's atmosphere. *Appl. Opt.,* **31,** 3068–3082.

——, W. F. Murphy, N. W. Walsh, and K. D. Evans, 1993: Temperature sensitivity of an atmospheric Raman lidar system based on a XeF excimer laser. *Opt. Lett.,* **18,** 247–249.